Soft Actuators Based on Spin-Crossover Particles Embedded in Thermoplastic Polyurethane

Yue Zan, Mario Piedrahita-Bello, Seyed E Alavi, Gábor Molnár, Bertrand Tondu, Lionel Salmon, Azzedine Bousseksou

ADVANCED INTELLIGENT SYSTEMS
Open Access
www.advintellsyst.com

Soft Actuators Based on Spin-Crossover Particles Embedded in Thermoplastic Polyurethane

Yue Zan, Mario Piedrahita-Bello, Seyed E. Alavi, Gábor Molnár, Bertrand Tondu, Lionel Salmon, and Azzedine Bousseksou**

Molecular spin-crossover (SCO) complexes are phase-change materials that develop large spontaneous strains across the thermally induced phase transition, which can be advantageously used in designing soft actuators. Herein, a bilayer bending cantilever, made of thermoplastic polyurethane (TPU) with embedded $[Fe(NH_2trz)_3](SO_4)$ SCO particles (25 wt%), is presented. The proposed actuator is fabricated by blade casting an SCO@TPU layer on a conducting Ag@TPU film to convert electrothermal input into mechanical response. Experiments are conducted to characterize the curvature of bilayer beams, which is then further analyzed using the Euler–Bernoulli beam theory. The beam curvature change, free transformation strain, and effective work density associated with the SCO are 0.11 mm^{-1}, 1.6%, and 1.25 mJ cm^{-3}, respectively. Further, the open- and closed-loop response of the actuator is investigated using a custom-built setup. The open-loop identification suggests that the actuator gain increases monotonously when the control current increases. This natural adaptive character can explain the drastically diminished response time in closed-loop proportional–integral–derivative control experiments (2–3 s). Finally, tracking experiments are carried out to evaluate the robustness of the actuator with and without payloads. The results for 30 240 endurance cycles reveal a mean positioning error of 0.8%.

1. Introduction

Recently, soft actuators have been increasingly considered for applications in various technological fields, such as soft robotics, artificial muscles, wearable technologies, medical devices, and smart textiles.[1–15] These devices are inspired by human muscles, which are agile, reconfigurable, physically adaptive, lightweight, and multifunctional. The development of new stimuli–responsive materials, including the optimization of their properties and their integration into actuator systems, plays a central role in this endeavor.[15–22] Among the different kinds of functional materials used in soft actuators, the most studied are electroactive polymers, gels, piezopolymers, shape memory polymers, and soft magnetic composites.[23–32] Each material has pros and cons and none of them can fulfill the numerous and sometimes even disparate technological requirements (e.g., mechanical compliance, high work density, efficiency, reliability, speed, accuracy, scalability, controllability). Depending on the physical mechanisms underlying the actuation, they can be operated by different stimuli, including electric fields, temperature, pressure, magnetic field, humidity, or light irradiation, but electrical current or tension are the most relevant due to their ease of use.[33,34]

Molecular spin-crossover (SCO) complexes of iron(II) ions exhibiting substantial volume change upon stimuli-induced switching between their high-spin (HS) and low-spin (LS) states appear promising candidates in this context.[35,36] Indeed, the SCO phenomenon is not only accompanied by a large spontaneous strain[37] (up to 22 vol%[38]) and associated large strain energy densities (up to a few tens of J cm^{-3}[36]), but provides also unique multifunctionality (concomitant change of mechanical, optical, caloric, and magnetic properties), multiresponsiveness (to temperature, pressure, light, and chemical stimuli), and large compositional and morphological versatility.[39–41] To enhance their processability, SCO compounds are frequently embedded into polymer matrices to form particulate composites.[42,43] Based on this approach, conventional bending bimorph actuators were recently fabricated in our team using SCO@polymer composites by means of solvent casting,[44] spray coating,[45] blade casting[46,47] and 3D printing.[48] Since nearly all SCO@polymer composite materials are electrically insulating, in practice, they are used in combination with a conducting material to achieve electrothermal actuation.[44,46]

Y. Zan, M. Piedrahita-Bello, S. E. Alavi, G. Molnár, L. Salmon, A. Bousseksou
LCC
CNRS & Université de Toulouse (UPS, INP)
31077 Toulouse, France
E-mail: lionel.salmon@lcc-toulouse.fr; azzedine.bousseksou@lcc-toulouse.fr

B. Tondu
LAAS
CNRS & Université de Toulouse (UPS, INSA)
31400 Toulouse, France

The ORCID identification number(s) for the author(s) of this article can be found under https://doi.org/10.1002/aisy.202200432.

DOI: 10.1002/aisy.202200432

In a recent paper,[46] we reported the detailed investigation of this type of SCO@P(VDF-TrFE)/Ag@P(VDF-TrFE) bimorph electrothermal actuators (P(VDF-TrFE) = poly(vinylidene fluoride- trifluoroethylene)). We have shown that the appropriate choice of SCO particle composition, concentration, and morphology allows for large bending movements. The actuators displayed excellent controllability, both in open- and closed-loop configuration,[49] positioning accuracy, and robustness. Since the performance of these actuators is related to the elastic compliances of the polymer matrix and the active SCO filler, it could be efficiently engineered by adjusting the stiffness ratio of the components. The main objective of the present work was thus to explore the design space provided by soft polymer matrices. To this aim we have chosen the polymer matrix TPU (thermoplastic polyurethane) for its easy processing[50–52] and its low Young's modulus compared to P(VDF-TrFE) (≈10 MPa vs. 1 GPa). The expectation is that in the soft TPU matrix, the SCO phenomenon gives rise to a higher effective strain and thus amplified bending movement. On the other hand, one may question whether the various attractive features of the actuator (work density, controllability, reproducibility, accuracy, resilience, etc.) can be preserved despite the drastic increase of elastic compliance.

2. Results and Discussion

2.1. Bilayer Film Characterization

In order to exploit the actuating performance of our SCO composite material, electrothermally actuated bilayer devices were built, which comprise an Ag@TPU layer with 70 wt% electrically conducting silver flakes and an SCO@TPU layer with 25 wt% (14 vol%) mechanically active $[Fe(NH_2trz)_3](SO_4)$ particles, both embedded in the same TPU polymer matrix forming monolithic samples. Transmission electron microscopy (TEM) and scanning electron microscopy (SEM) images revealed ≈1 µm-sized silver flakes and 1–2 µm-long, rod-shaped SCO particles with an aspect ratio of ≈10 (see Figure S7 and S11, Supporting Information). The $[Fe(NH_2trz)_3](SO_4)$ complex we used in this study belongs to the iron(II)-triazole family of compounds and it consists of 1D coordination networks $[Fe(NH_2trz)_3^{2+}]_n$ packed in a hexagonal lattice, whereas the SO_4^{2-} counteranions are located in the voids between the chains (see inset in **Figure 1**).[53] This compound was chosen for its large transformation strain (≈5 vol%) and abrupt spin transition above room temperature.

The thermal behavior of the pure and composite materials was investigated using differential scanning calorimetry (DSC) (see Figure S4–S6, Supporting Information). The material 'TPU 85 shore A' behaves as an amorphous thermoplastic elastomer. It displays only a small and broad peak around 170 °C, which is related to the disordering of crystallites with relatively short-range order (the first small peak at lower temperature arises due to the additives in the polymer).[54] This behavior is not considerably altered by the SCO filler, which indicates that the properties of the polymer are preserved in the composite. Similar to the DSC trace of the pure SCO complex, the composite sample exhibited endo- and exothermic peaks, which accompany the spin transition upon heating and cooling, respectively. The peak areas are proportional to the quantity of the SCO filler in the composite (25 wt%) and the peak temperatures shift only slightly (in cooling mode), confirming the results of the magnetic measurements in that the spin transition remains virtually unaltered by the polymer matrix (see Figure S3, Supporting Information).

Freestanding bilayer films were constructed layer by layer on an anti-adhesive surface by a blade-casting method while controlling the temperature of the substrate and the height of the blade (see Figure 1 and the experimental section for the bilayer actuator fabrication). Overall nine bilayer films were fabricated, among which six samples (**B1–B6**) were aimed to be identical (to check reproducibility) and three samples (**B7–B9**) were made using the "reverse process," in which first the SCO@TPU layer was cast, followed by the Ag@TPU.

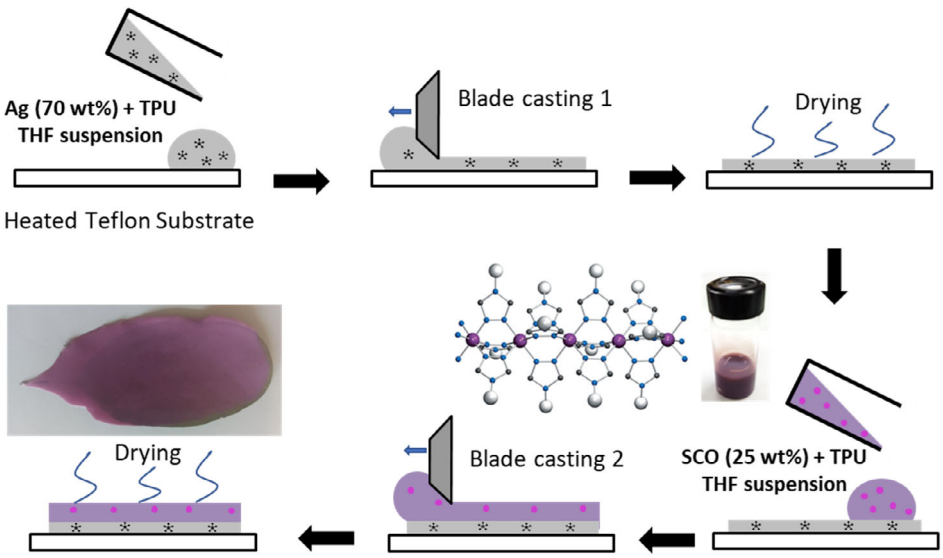

Figure 1. Scheme of the blade-casting process to produce the bilayer devices **B1–B6**. The chemical structure of the SCO complex and photographs of the SCO@TPU suspension and the resulting Ag@TPU/SCO@TPU bilayer film are also shown.

Representative SEM images for the bilayer film **B1** are shown in **Figure 2** (see also Figure S8-S13, Supporting Information, for complementary images). Figure 2a represents the image of the surface of the SCO@TPU layer and reveals a homogeneous dispersion as well as some preferential orientation of the rod-shaped SCO particles, roughly along the direction of the cast. This finding was also substantiated by examining the SCO@TPU layer cross section obtained following both parallel and perpendicular cuts with respect to the direction of the blade movement (see Figure S12, S13, Supporting Information). Indeed, for the parallel cross section we can see a higher proportion of entire rods, while for the perpendicular cross section mostly sections of rods can be seen. Such preferential alignment of anisotropic particles during blade casting is not unexpected and indeed has been already reported in several cases.[55–57]

Figure 2b displays the bilayer cross section showing distinctly the two layers of the film (see also Figure S14–S18, Supporting Information, for quantitative energy-dispersive X-ray spectroscopy, EDX, analyses). From this image, the estimated thickness is 110 and 100 μm for the Ag@TPU and SCO@TPU layers, respectively, in agreement with macroscopic measurements performed with a micrometer. As can be expected, the high mass density of silver causes the silver flakes to migrate to the bottom of the Ag@TPU layer. On one hand, this phenomenon leads to a more continuous TPU interface between the two layers, ensuring good mechanical coupling and impeding delamination during repetitive thermal cycling, which is a frequent flaw in multilayer bending devices. Indeed, thanks to our monolithic design using a common polymer matrix for the strata, we have never observed delamination upon consecutive thermal cycles in any of our devices. On the other hand, the migration and agglomeration of the silver flakes at the surface of the conductive layer was also favorable for the formation of a percolative network. The adequate silver loading to reach a sufficient electrical conductivity (above the percolation threshold), necessary for the Joule heating of the device, was ≈70 wt%. It is interesting to note that for similar Ag@P(VDF-TrFE) composites, percolation was reached at 60 wt%, which corresponds to the same volume fraction (≈0.2) of Ag particles.[46] Importantly, when the conductive Ag@TPU layer was cast on top of the SCO@TPU layer (**B7**–**B9**), the electrical resistance of the device was systematically higher (≈6–18 Ω) in comparison with the opposite configuration (**B1**–**B6**), displaying resistance values between 0.5 and 4 Ω (see Table S1, Supporting Information). Whatever the sample, we noted also that annealing overnight at 105 °C tended to increase the electrical conductivity slightly. As an example, for the best conductive sample the resistance decreased from 1 to 0.5 Ω. Finally, to study the influence of the orientation of the particles on the actuation performance, devices with specific shapes (rectangular beam and U-shaped actuators) were cut from the as-prepared bilayer films both with parallel (**B**//) and perpendicular (**B**⊥) orientations with respect to the direction of the movement of the blade used for film casting (see Figure S19, Supporting Information, for more explanation).

2.2. Thermal Actuation of Bilayer Beams in a Fluid Bath

For the quantitative analysis of the bending behavior of the bilayer composite films, rectangular beams were cut from sample **B1** (14 vol% SCO) in both orientations. For comparison, we have also fabricated a bilayer beam of similar dimensions, but with a higher content of SCO particles (50 wt% = 28 vol% - sample **C**) and another one with a similar particle composition, but in a stiffer P(VDF-TrFE) matrix (15 wt% = 14 vol%: sample **D**). These beams were then clamped on one end and immersed into a fluid bath to ensure homogenous temperature upon heating and cooling. The stresses generated in the beam due to the thermal strain mismatch of the two layers gave rise to a sizeable bending moment at the SCO. The resulting beam deflections were then measured as a function of the temperature using a video camera (**Figure 3**, see also the Supporting Information). The first heating–cooling cycle has always led to some irreversible changes, but the following cycles were found reversible. The curvatures of the beam recorded at 100 and 20 °C on the second heating ($\kappa_{100\,°C}$, $\kappa_{20\,°C}$) are given in **Table 1** for each sample. First, one can note the substantial difference between the bending behavior of samples **B**// and **B**⊥, in agreement with the observed preferential alignment of the particles along the casting direction. There is also an obvious decrease of the beam deflection amplitude when replacing the soft TPU matrix by the stiffer P(VDF-TrFE). On the other hand, the impact of the increased particle concentration (from 14 to 28 vol%) in the TPU matrix

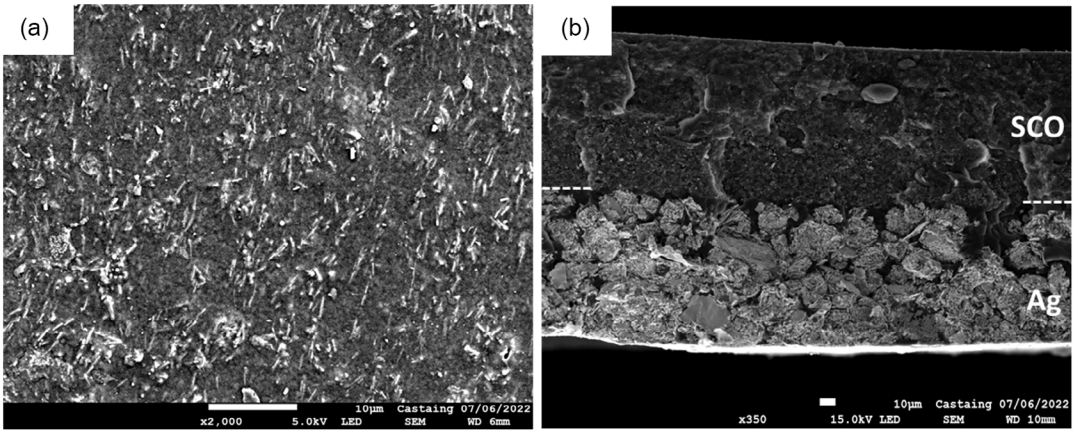

Figure 2. SEM images showing a) the surface of the SCO@TPU layer and b) the bilayer cross section for sample **B1**.

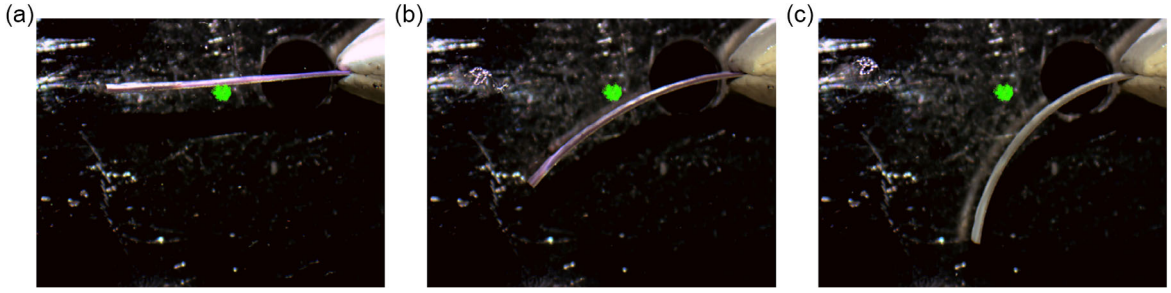

Figure 3. Movement of a rectangular bilayer strip (**C**//) upon the spin transition when heating from 20 to 100 °C. a) Initial, b) end of first cycle, and c) end of second heating.

Table 1. Experimental and calculated parameters from bilayer beam bending experiments for selected actuator devices.

Sample	**B1**//	**B1**⊥	**C**//	**D**//
Conducting layer (*a*)	Ag@TPU 20 vol%	Ag@TPU 20 vol%	Ag@TPU 20 vol%	Ag@ P(VDF-TRFE) 20 vol%
SCO layer (*b*)	SCO@TPU 14 vol%	SCO@TPU 14 vol%	SCO@TPU 28 vol%	SCO@P(VDF-TRFE) 14 vol%
E_a [MPa]	50	50	50	625
E_b [MPa]	112	64	352	462
α_a [kK^{-1}]	0.1	0.1	0.1	0.52
α_b [kK^{-1}]	0.105	0.14	0.134	0.15
h_b [µm]	100	100	90	60
h_a [µm]	110	110	60	53
L [mm]	8.38	10.33	8.34	6.88
$\kappa_{20\,°C}$ [mm^{-1}]	0.0	0.0	0.0949	−0.0308
$\kappa_{100\,°C}$ [mm^{-1}]	0.1134	0.0604	0.1633	0.0528
ε^{SCO}_{comp} [%]	1.616	0.765	1.898	1.196
ε^{SCO}_{exp} [%]	1.65	0.85	1.95	0.9
W/V [mJ cm^{-3}]	1.25	0.252	4.59	0.729
Π [mJ cm^{-3}]	14.61	1.87	63.43	33.04

is less clear: the curvature change $\Delta\kappa$, is reduced, but this sample exhibits a large initial bending.

The cantilever curvature changes were further analyzed using the conventional Euler–Bernoulli (EB) beam theory (see details in the Supporting Information).[58] In a first step, from the measured change of curvature, we calculated the free transformation strain in the SCO@TPU layer, ε^{SCO}, that is, the strain which would arise during the SCO if the film was not attached to the Ag@TPU layer. This value is obtained from the following relationship (see also the Supporting Information)

$$\kappa = \frac{12[(\alpha_b - \alpha_a)\Delta T + \varepsilon^{SCO}](1+m)^2 + \kappa^0 h(1+mn)\left(m^2 + \frac{1}{mn}\right)}{2h\left[3(1+m)^2 + (1+mn)\left(m^2 + \frac{1}{mn}\right)\right]} \quad (1)$$

where $m = \frac{h_a}{h_b}$; $n = \frac{E_a}{E_b}$, $h = h_a + h_b$, h_i is the thickness of each layer, E_i is the Young's modulus of each layer, α_i is the thermal expansion coefficient of each layer, κ^0 is the curvature of the beam at the end of first heating/cooling cycle, and $\Delta T = 80\,°C$ is the temperature range of interest. As shown in Table 1, the computed values of ε^{SCO}_{comp} are in reasonably good agreement with the transformation strain assessed using thermal expansion measurements, ε^{SCO}_{exp}, which are reported in ref. [59]. This result provides confidence for our numerical approach. Nevertheless, one has to keep in mind that uncertainties on the absolute values of input parameters (e.g., Young's moduli) are typically of 10–20%. The computed stress and strain profiles across the thickness of the bilayer are shown in **Figure 4**. When the SCO@TPU layer in contact with the Ag@TPU layer expands due to the SCO phenomenon, it induces bilayer curvature, which results in strains that differ from the transformation strain. Due to the large value of ε^{SCO}, virtually the whole beam experiences stretching (positive strain), which decreases linearly from the SCO@TPU free surface to the Ag@TPU free surface. The neutral (i.e., zero strain) axis is found close to the latter. Contrary to the strain, the stress is not continuous across the interface of the two layers (due to the discontinuity of the Young's modulus): the SCO@TPU layer is under compression (negative stress),

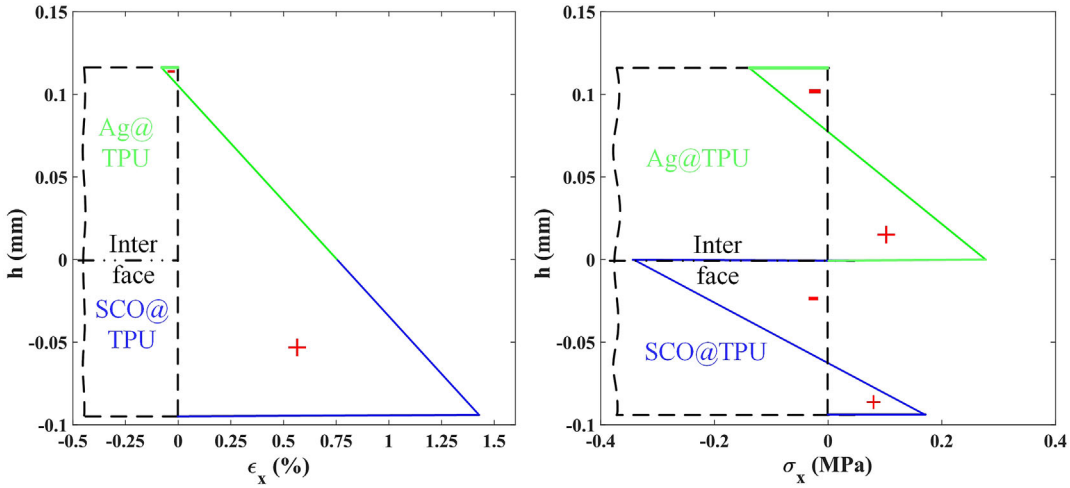

Figure 4. Strain and stress profiles across the height at the free end of the bilayer cantilever **B1**//.

whereas the Ag@TPU layer is under tension. The interfacial stress, given by the difference in stress in the two layers around the interface, is ≈0.65 MPa. This relatively low interfacial stress explains, at least partly, that no delamination has been observed in our devices over numerous actuation cycles. The stress and strain values within the entire structure remain below the plastic deformation limit of the composites. Indeed, plastic deformation was observed only during the initial heating–cooling cycle, after which the materials are stabilized and, possibly, strain hardened to a higher modulus. As such, they are no longer driven outside the elastic limit.

The two sources for producing deformation in the bilayer beam are 1) the difference in the thermal expansion coefficients of each layer and 2) the transformation strain in the active layer. In our case, the contribution of the thermal expansion coefficient mismatch is negligible. Then, the total potential energy per volume of the bilayer due to the SCO is given by

$$\Pi = \frac{1}{2} E_{SCO} (\varepsilon^{SCO})^2 \tag{2}$$

One can see that the potential energy of the TPU composite is reduced with respect to the stiffer P(VDF-TrFE) matrix; this is the tradeoff for the higher actuation amplitude. It should be noted also that the total strain energy density of the beam, which actually produces work in the beam structure, is just a portion of the above potential. It was calculated from the computed values of stress, σ, and strain, ε, integrated over the entire volume of the beam as

$$W/V = \frac{\frac{1}{2}\int_V \sigma \varepsilon \mathrm{d}V}{V} \tag{3}$$

where V is the volume of the beam. As shown in Table 1, typically only 10 % of the potential energy is used to produce work in our beam bending experiments. However, it is important to note that under different loading and boundary conditions, one might reach different efficiencies. For example, if a blocking force is applied to the free end of the beam, the effective work density will be significantly higher.

2.3. Electrothermal Actuation and Identification in Open-Loop Conditions

Electrothermal actuation measurements were performed by cutting the bilayer devices in a "U shape" and fixing one end on the measuring bench, whereas the other end was left to bend either freely or with payloads. The actuation was achieved by Joule heating the device and the resulting change of the tip position was detected by a noncontact, optical position sensor (**Figure 5**a). In situ temperature maps of the devices were obtained by an infrared camera and photographs of the device are taken using a video camera. A custom-made Labview program allowed us to follow the tip position, the current intensity, and the device electrical resistance as a function of the time. The devices were tested both in open- and closed-loop control (Figure 5b). In open-loop configuration, we applied at $t = 0$ a current bias and we followed the tip position, whereas in closed-loop configuration, we defined the target position as a function of time and we used a standard proportional–integral–derivative (PID) control scheme to drive the current source, based on the positioning feedback from the optical sensor. We discuss below the detailed investigation of device **B1**, but quantitatively comparable results were obtained with five other samples in terms of actuation amplitude (both for parallel and perpendicular cuts), proving the robustness of the device fabrication process (see Figure S26 and Table S1, Supporting Information).

A typical open-loop experiment is shown in Figure 5c. On the application of the current bias (2 A), the temperature of the device increases, which is also manifested by an increase of its electrical resistance. Then, the thermally induced spin transition in the device leads to the bending of the cantilever toward a steady-state position (9.0 mm). When the current excitation is stopped, it returns to its initial position. We shall note that after the very first heating, the actuator does not come back exactly to its initial position (see Figure S20, Supporting Information). This behavior, also seen in the DSC, magnetic and beam bending measurements (vide supra), corresponds to a 'run-in effect', which can be attributed to the loss of solvent and/or irreversible microstructural changes for both the filler and the TPU matrix.

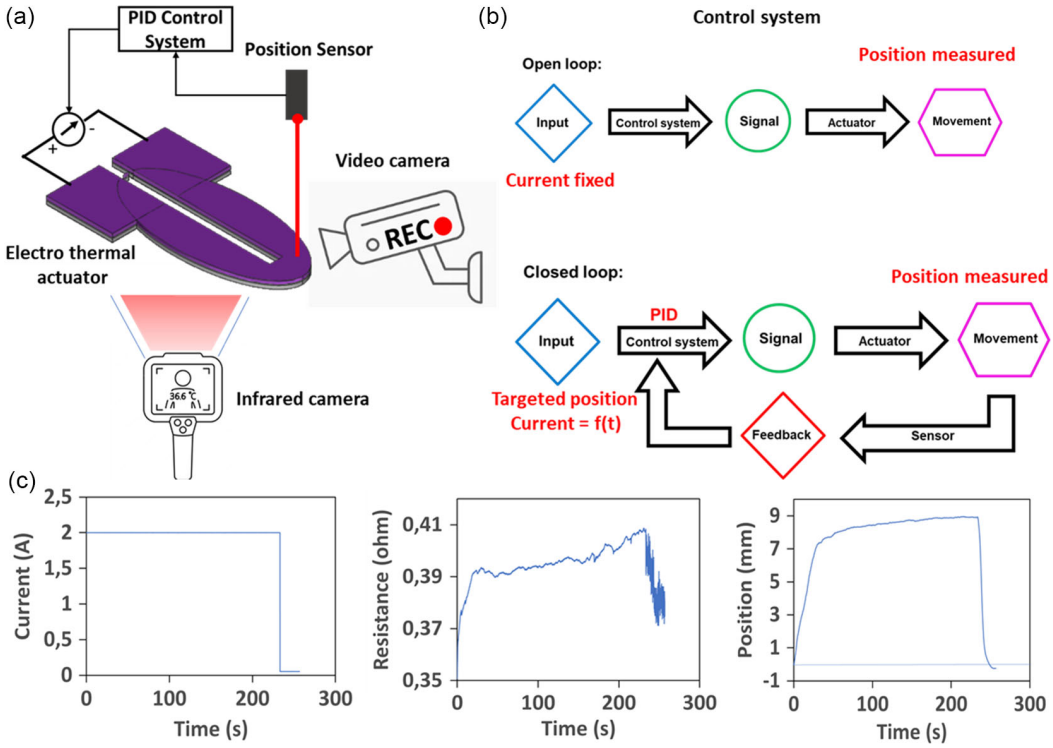

Figure 5. a) Scheme of the actuator test bench incorporating a current source, a position sensor, a video camera, an infrared camera, and a PID control system. b) Block diagrams of the open- and closed-loop control systems. c) Typical measurement data for an open-loop experiment (first heating) with device **B1**//: the driving current intensity, the device electrical resistance, and the tip position of the actuator as a function of time.

Nevertheless, following this first heating, the device becomes stabilized and returns precisely to its initial position regardless of the applied current intensity (see Figure S21, Supporting Information). The open-loop actuation response of samples **B1**// and **B1**⊥ is shown in **Figure 6**a,b, respectively, for various current intensities. In order to avoid damage of samples by overheating, the current bias was limited to values below 1.9 A. Representative temperature maps are displayed in Figure 6c, whereas Figure S22 and S23, Supporting Information, compile the thermal images for each applied current both for **B1**// and **B1**⊥. As it can be expected, the temperature is always the highest near the cantilever tip. One can note also the absence of hot/cold spots denoting a homogeneous dispersion of the silver particles. For both devices, the increase of the current bias tends to increase the amplitude of the displacement (Figure 6a,b), which is obviously related to the thermal expansion mismatch of the two layers. The combined analysis of the thermal images and the actuation response for increasing current reveal that the major contribution to this mismatch comes from the spin transition and the effect of ordinary thermal expansion remains negligible, ca. one order of magnitude smaller (Figure S24, Supporting Information). This observation shows that the strain associated with the SCO phenomenon plays a crucial role in the movement of the actuators.

In the case of sample **B1**//, the highest displacement amplitude is 9.0 mm for an input current of 1.8 A and a further increase of the current to 1.85, 1.9, and 2.0 A does not lead to any significant movement. For a similar maximum current bias (1.78 A), sample **B1**⊥ exhibits a tip displacement of only 5 mm. This difference in the bending amplitude of the parallel and perpendicular cut samples can be also visually depicted in Figure S25, Supporting Information. These results are in agreement with the beam bending experiments shown in Figure 3 and show again the importance of the particle orientation on the actuating behavior. At this point, it is worth noting that contrary to samples **B1**–**B6** (processed as SCO@TPU on top of Ag@TPU), significant inhomogeneity of the silver filler was inferred from the thermal images for devices **B7**–**B9** (processed as Ag@TPU on top of SCO@TPU), revealing large zones with disparate temperatures. Consequently, only a reduced fraction of the SCO particles exhibits spin transition, which leads, in turn, to a decrease of the actuation amplitude (see Figure S27 and S28, Supporting Information). These results highlight the requirement to build homogeneous films and the importance of seemingly minor details in the fabrication process.

These open-loop experiments allow us to characterize the response time (RT) of the actuator, corresponding to the time needed to reach definitively the 5% margin of position error with respect to the steady-state position. To reach different positions, RT values between 20 and 50 s were observed, independently of the samples. Such a long response time represents obviously a limitation for potential applications. This shortcoming can be greatly improved, however, using closed-loop feedback control via a PID controller (vide infra). In a previous study,[49] we showed the relevance to identify the time response of similar bending actuators under the form of a simple, overdamped

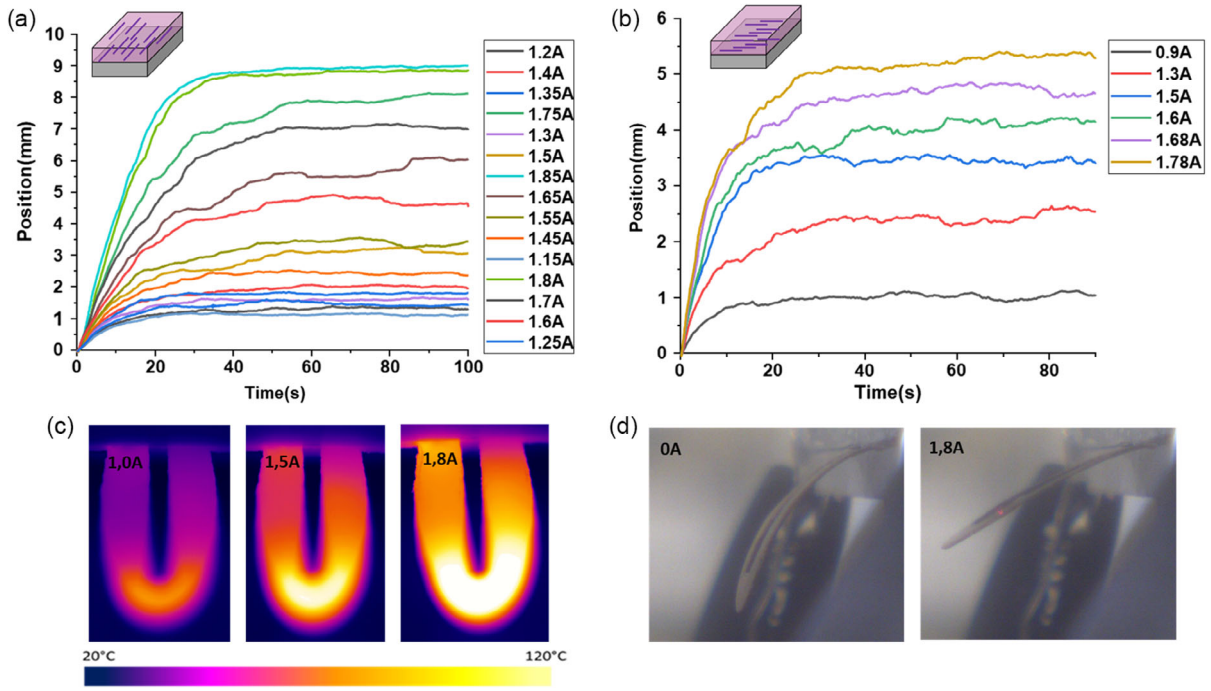

Figure 6. Open-loop actuation response to a step current input for devices a) **B1**// and b) **B1**⊥. c) Temperature maps of the device for selected current bias values. d) Photographs of the actuator **B1**// for 0 and 1.8 A applied current.

second-order model, whose parameters were dependent on the value of the step current. In the case of sample **B1**//, after various trials, and using the numerous recorded step responses, we considered a second-order model including an additional nonlinear viscous component, as follows: $x + a\dot{x} + b(\dot{x})^2 + c\ddot{x} = KI$ where I is the control current, x is the actuator position, K the actuator gain, and a, b, c are model parameters. The resulting identification is shown in Figure S29, Supporting Information. It is important to note that the model parameters can be considered to be either almost constant (for a and c) or varying in a limited range (for b), but the gain K increases in the whole current range, from a value of ≈1 to ≈5 mm A^{-1}, as illustrated in Figure S33a, Supporting Information. In the case of the **B1**⊥ sample, we consider a simple linear first-order model as follows: $x + T\dot{x} = KI$, where T is a time constant. By comparison with the **B1**// sample, the difficulty to model multiple slope variations in this sample leads us to limit this identification process to this simple model. The resulting identification in the [0.9–1.7 A] range is shown in Figure S30, Supporting Information with the associated variations of T and K. The gain K varies in a roughly linear way between ≈1 and 3 mm A^{-1}, while T varies between ≈5.5 and 7.5 s, in a way, which is more difficult to characterize.

2.4. Electrothermal Actuation and Tracking in Closed-Loop

Strictly speaking, the resulting open-loop identification, either in the form of a first-order or a second-order system, has no linear form since, beyond the presence of a nonlinear viscous component, at least one identified parameter (i.e., the gain) varies with the current I. Nevertheless, following our previous results,[49] the use of a simple linear PID (i.e., with constant gains) was considered for closed-loop control. The PID is the one implemented in the LabVIEW software: the output current $I(t)$ is generated according to the following equation: $I(t) = k_c[e(t) + T_d\dot{e}(t) + \left(\frac{1}{T_i}\right)\int_0^t e(t)dt]$, where $e(t)$ is the position error, k_c is the PID gain and T_d, T_i are, respectively, derivative and integral parameters. In the case of a nonlinear first-order system controlled by a PID, and in the case of a nonlinear second-order one controlled by a PD, the stability of the closed-loop system can be easily derived by means of Lyapounov's movement stability theory.[60] In the case of the **B1**// sample, the integrator component T_I is, however, necessary in order to cancel the steady-state error resulting from the drift peculiar to this type of actuator. The resulting third-order nonlinear system can then be instable for a certain choice of the T_I parameter. In the framework of this article, we did not try to determine the stability conditions. We checked it in practice and we can say that after first tuning of the k_c and T_d parameters, the T_I parameter can be progressively increased until nondesired excessive oscillations occur. It is important to note also that in steady state the maximum current is limited to ≈1.9 A, whereas higher current values (up to 3.15 A) are admissible in a closed-loop control for a few seconds.

Considering this identification and slightly refining the PID by hand tuning, the bilayer actuator **B1**// was set to move to a series of target positions between 7 and 3 mm (**Figure 7**a). While the time response in open-loop is equal to several tens of seconds, the time response to maintain 95% of a given command in closed-loop now varies from ≈1.6 s for a 3 mm step to ≈2.5 s for a 7 mm step. Similar results were obtained for the actuator **B1**⊥ for displacement positions between 2 and 4 mm (Figure S31

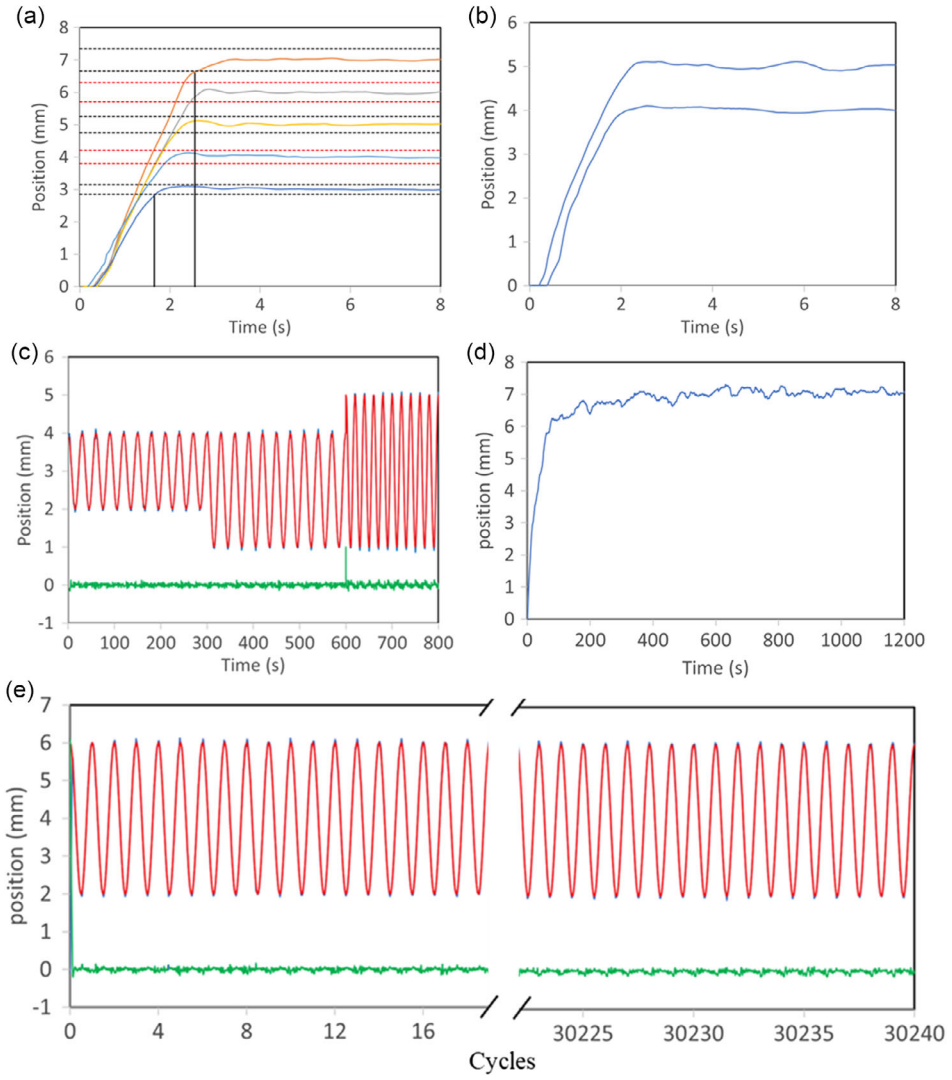

Figure 7. Actuator control experiments with sample **B1**//. a) Closed-loop control of the device with various target displacements (3, 4, 5, 6, and 7 mm). Dotted horizontal lines indicate the zone of ±5% error relative to the target displacement. The vertical lines indicate the response time range. b) Closed-loop control of the device for a target displacement of 4 and 5 mm with 204 mg load. c) Closed-loop control of the device in response to desired sine waves with varying control parameters (target displacement, amplitude, and frequency). The error between the target position and the actuator position is also shown. d) Open-loop actuation of the device over a period of 20 min ($I = 1.7$ A). e) Closed-loop sinusoidal actuation of the device at the beginning and at the end of 30 240 cycles (7 days, 0.05 Hz).

and S32, Supporting Information). Such a result is particularly remarkable since, in the case of a linear system, one can expect that a well-tuned PID control makes possible to reduce the open-loop system response by a factor of about 2.[61] Such surprising decrease of the response time by a factor of ≈10–20 was already observed in similar bilayer actuators constructed with a P(VDF-TrFE) matrix[49] and appears thus as a general characteristics of such systems. Using the approach we developed in ref. [49], we simulated the closed-loop PID step response—including current control saturation—with the considered identified open-loop model (Figure S33, Supporting Information). Let us note that the pure time delay (≈0.2–0.3 s) was neglected in the open-loop identification, but it has to be considered in these closed-loop simulations. Because no open-loop identification is feasible beyond 1.9 A, considering the same second-order nonlinear model, the choice of the *K*, *a*, *b*, and *c* parameters becomes speculative within the broad current range [0–3.15 A] used in closed-loop experiments. Therefore, for the *a*, *b*, *c* parameters, we considered constant mean values within the identification current range, extended to the full control input range. For the *K*-parameter, we postulated a steady increase, defined by linear interpolation between identified values and by segments with increasing slopes outside this identification range. As a consequence, the resulting $K(I)$ curve has a concave shape (see Figure S33a, Supporting Information). As shown in Figure S33c,d, Supporting Information, such a concave $K(I)$ profile can indeed explain the drastic decrease of the response time with values very close to the experimental ones (≈1.65 s for a

3 mm-step and 2.8 s for a 7 mm-step). In the case of the **B1**⊥ sample, we proceeded in a similar manner: a mean value was considered for the time constant *T*, whereas the actuator gain was linearly interpolated between the recorded data in the [0.9–1.7 A] range and extended with constant slopes. This approach led to a roughly linear variation of the gain *K* within the full [0–3.15 A] range (see Figure S30d, Supporting Information). The comparison with the simulated PID and the experimental closed-loop step response is given in Figure S34, Supporting Information. As in the case of the **B1**// sample, the simulated response times are very close to the experimental ones. We also give in Figure S34b, Supporting Information, the comparison between the simulated and experimental current intensities in the case of the 4 mm desired step position. The ensemble of these results suggests more dry friction-like phenomena in the case of the **B1**⊥ sample, as highlighted by multiple "stops" during the 4 mm desired step position.

On the whole, as a preliminary conclusion, we can say that the considered actuator with its increasing $K(I)$ profile gives a natural adaptive character to a simple, saturated linear PID control. During a desired position step, the saturation in current leads to a high control gain, which is automatically reduced in the neighborhood of the desired position by a drastic reduction of the actuator gain.

These closed-loop experiments were repeated with a payload. The maximum load that these devices (**B1**// and **B1**⊥**)** could handle was 204 mg, which represents 3 times the weight of the actuator itself (Figure 7b, S31 and S35, Supporting Information). The response times similar to those measured without load prove the ability of the actuator to move in a controllable manner with various loads. To further explore the closed-loop control, the actuator was driven using various sinusoidal waveforms of different amplitudes and frequencies (Figure 7c, S31 and S36, Supporting Information). The actuator followed these commands accurately, with a maximum error of 1.5% and average error of 0.6% of the target position, even being able to follow a change in sinusoidal parameters. To evaluate the long-term stability of the control, the actuator was oscillated with a period of 20 s, at an amplitude of 4 mm, during 7 days for 30 240 actuation cycles. As shown in Figure 7e, the device showed virtually no sign of fatigue and was able to pursue the command with a standard deviation of ≈35 μm through the entire experiment, indicating an important operating life-cycle. The reproducibility of these results was also demonstrated by similar experiments conducted on samples **B2**// and **B4**//, shown in Figure S37 and S38, Supporting Information. It is important to note that, besides the obvious benefits of the closed-loop control, the actuator is indeed intrinsically robust. To highlight this resilience, the actuator was subjected to a constant current of 1.7 A during 20 min while following its position, revealing negligible drift (Figure 7d). At this point, one should note, however, that depending on the temperature reached, the time spent at that temperature, and the applied load, creep and irreversible deformation might occur in the TPU matrix and these experimental limits must be always carefully examined. Closed-loop Dirac pulse experiments were also conducted for sample **B4**//. The 5 mm-fixed equilibrium position was well maintained upon successive antagonist Dirac pulses from 4 to 1 mm and from 6 to 8 mm (Figure S39, Supporting Information). In order to further probe the stability of the response of our actuators, we carried out also a second series of open-loop experiments 2 weeks after the first series of extensive experiments (including open-loop, closed-loop, tracking, and payload experiments). This result is shown in Figure S40, Supporting Information, and does not reveal any significant difference with the first series of experiments, in agreement with a SEM analysis, carried out after the two series of experiments, showing no sign of interface cracks/delamination within the bilayer (see Figure S41, Supporting Information).

3. Conclusion

We have shown that the soft polymer matrix TPU enables the reproducible construction of bimorph, bending devices actuated by embedded SCO particles (15 vol%). The soft matrix significantly enhances the actuation strain and bending amplitude, when compared to similar devices made with a stiffer polymer matrix. In closed-loop control, the device can follow trajectories with different amplitudes and frequencies with precision and long-term durability. Open-loop identification of the devices highlights their naturally adaptive character, which can explain the observed fast response times (2–3 s) under PID control. TPU being among the most commonly used 3D printing filaments, this work provides a pathway for fabricating complex soft morphing structures with 4D printing capability.

4. Experimental Section

Sample Characterization: Elemental analyses of C, H, and N were performed after combustion at 850 °C using IR detection and gravimetry by means of a Perkin–Elmer 2400 series II device. Thermogravimetric analyses (TGA) were conducted in an inert nitrogen atmosphere using a Mettler Toledo 3+ thermal analyser. DSC measurements were carried out on a Netsch DSC 3500 Sirius instrument under nitrogen purging gas (20 mL min^{-1}) at a heating/cooling rate of 10 K min^{-1}. Temperature and enthalpy were calibrated with respect to the melting peak of a pure indium sample. The size and morphology of the SCO particles were determined by TEM using a JEOL JEM-1011. TEM samples were prepared by placing a drop of the particles (suspended in ethanol) on a carbon-coated copper grid. SEM images were acquired using a JEOL JSM 7800 F Prime operated at 5 kV. Samples for SEM were prepared by breaking the film cooled by liquid nitrogen and metallizing the cross-section with Pt. Magnetic susceptibility data were collected with a Quantum Design MPMS-XL SQUID magnetometer at heating and cooling rates of 2 K min^{-1} in a magnetic field of 1 kOe. The magnetic data were corrected for the diamagnetic contribution.

Synthesis of the Spin Crossover Complex: All reagents were purchased from Sigma Aldrich and used without further purification. $[Fe(NH_2trz)_3](SO_4)$ was synthesized by dissolving 8.19 g of 4-NH_2-1,2,4-triazole in 18 mL of water. In a separated flask, 9 g of $FeSO_4{\cdot}7H_2O$ was dissolved in 18 mL of water with some ascorbic acid. The iron solution was added slowly to the triazole ligand solution and the mixture was stirred for 36 h at room temperature resulting in a pink precipitate. The product was filtered under vacuum and was purified by three successive ethanol washing/centrifugation cycles resulting in 10.9 g of a pink solid (85% yield). TGA revealed the inclusion of 0.5 molecules of water and the thermal stability of the complex up to ≈250 °C (see Figure S1, Supporting Information). Elemental analyses calculated for $[Fe(NH_2trz)_3](SO_4){\cdot}0.5H_2O$ ($Mw = 412.5$ g mol^{-1}): C, 17.5; H, 3.1; N, 40.7%. Found: C, 17.4; H, 2.5; N, 40.2%. The thermal variation of the magnetic susceptibility, shown in Figure S2, Supporting Information, revealed

abrupt spin transitions at 341 and 332 K for heating and cooling, respectively, in agreement with previous reports.[47,53,62]

Fabrication of the Bilayer Actuator Devices: TPU 85A was supplied by BASF. The conductive Ag@TPU composite layer was prepared by dispersing 10 μm Ag flakes (1114 mg) in THF (1.8 mL) in an ultrasonic bath for 20 min. Then, TPU (476 mg) was added and dissolved at 40 °C, while gently stirring the suspension for 30 min. The resulting suspensions were blade cast at a height of 1 mm on a heated Teflon surface at 40 °C and kept at this temperature for 20 min, until the composite was dry, obtaining in a reproducible manner films of ≈110 μm thickness. The second layer, consisting of an SCO@TPU composite, was prepared by dispersing the SCO complex (172 mg) in THF (3 mL) in an ultrasonic bath for 20 min. Then, TPU (520 mg) was added and dissolved at 40 °C, while gently stirring the suspension for 30 min. The resulting suspensions were then blade cast at a height of 1 mm on top of the dry Ag@TPU layer at 40 °C and kept at this temperature for ≈1 h, until the bilayer composite was completely dry. Reproducible SCO@TPU layers with ≈100 μm thickness were obtained. The bilayer films were finally annealed at 105 °C for 12 h. A series of six bilayer samples (**B1**–**B6**) were fabricated using the same experimental conditions. Three further bilayers (**B7**–**B9**) were also prepared in identical experimental conditions, except that the first deposited layer was the SCO@TPU. Bilayer devices with size $30 \times 20 \times 0.15$ mm^3 were then cut into a U-shape using a Snapmaker 2.0 A250 laser cutter. The device thickness was measured with a Mitutoyo precision micrometer at several places on each actuator and a mean value of 210 μm was obtained with a standard deviation of 40 μm. The thermal variation of the magnetic susceptibility for the SCO@TPU composite film, shown in Figure S3, Supporting Information, revealed a fully complete spin transition at 342 and 336 K in the heating and cooling modes, respectively. This means that the SCO properties of the iron complex were not altered sizably by the TPU matrix.

Actuator Test Bench: Position tracking of the actuator devices was performed using a Micro-Epsilon opto-NCDT 2300 laser triangulation system. Electrothermal heating of the samples was achieved by a Keithley 2420 source-meter unit. The LabVIEW software was used for controlling the sample movement both in open-loop and closed-loop conditions. For the open-loop control of the sample, a current bias in the range between 0.3 and 1.9 A was applied in a stepwise manner. The duration of the step (typically 100 s) was set to ensure reaching the steady state. Due to the risk of damage to the sample by exposure to high temperatures for such long periods, no open-loop identification was performed beyond 1.9 A. On the other hand, the closed-loop control program made possible a current control until 3.15 A for short time windows. The closed-loop control program allowed also for different positioning signals, including steps and sine waves, with the possibility of changing both frequency and amplitude during the movement. The temperature of the samples was analyzed via infrared thermal imaging using a Micro Epsilon 640 Thermal Imager. Images during the actuation process were recorded with a Moticam CMOS camera.

Supporting Information

Supporting Information is available from the Wiley Online Library or from the author.

Acknowledgements

This project has received funding from the European Research Council (ERC) under the European Union's Horizon 2020 research and innovation programme (grant agreement No. 101019522). Y.Z. thanks the China Scholarship Council for a PhD grant.

Conflict of Interest

The authors declare no conflict of interest.

Data Availability Statement

The data that support the findings of this study are available in the supplementary material of this article.

Keywords

actuator identification and control, bilayer beams, polymer composites, soft actuators, spin crossovers

Received: December 12, 2022
Revised: February 1, 2023
Published online:

[1] D. Rus, M. Tolley, *Nature* **2015**, *521*, 467.
[2] G. M. Whitesides, *Angew. Chem. Int. Ed.* **2018**, *57*, 4258.
[3] J. D. Madden, *Science* **2007**, *318*, 1094.
[4] G. Alici, *MRS Adv.* **2018**, *3*, 1557.
[5] S. Kim, C. Laschi, B. Trimmer, *Trends Biotechnol.* **2013**, *31*, 287.
[6] L. Hines, K. Petersen, G. Z. Lum, M. Sitti, *Adv. Mater.* **2017**, *29*, 1603483.
[7] Y. Yang, Y. Wu, C. Li, X. Yang, W. Chen, *Adv. Intell. Syst.* **2020**, *2*, 1900077.
[8] N. El-Atab, R. Mishra, F. Al-Modaf, L. Joharji, A. Alsharif, H. Alamoudi, M. Diaz, N. Qaiser, M. Hussain, *Adv. Intell. Syst.* **2020**, *2*, 2000128.
[9] Ankit, T. Yan King Ho, A. Nirmal, M. Rameshchandra Kulkarni, D. Accoto, N. Mathews, *Adv. Intell. Syst.* **2022**, *4*, 2100061.
[10] L. Garcia, G. Kerns, K. O'Reilley, O. Okesanjo, J. Lozano, J. Narendran, C. Broeking, X. Ma, H. Thompson, P. Njapa Njeuha, D. Sikligar, R. Brockstein, H. M. Golecki, *Micromachines* **2022**, *13*, 28.
[11] S. Zaidi, M. Maselli, C. Laschi, M. Cianchetti, *Curr. Rob. Rep.* **2021**, *2*, 355.
[12] M. Li, A. Pal, A. Aghakhani, A. Pena-Francesch, M. Sitti, *Nat. Rev. Mater.* **2022**, *7*, 235.
[13] Y. Hao, S. Zhang, B. Fang, F. Sun, H. Liu, H. Li, *Chinese J. Mech. Eng.* **2022**, *35*, 37.
[14] Y. Chen, Y. Yang, M. Li, E. Chen, W. Mu, R. Fisher, R. Yin, *Textiles* **2021**, *1*, 283.
[15] I. Apsite, S. Salehi, L. Ionov, *Chem. Rev.* **2022**, *122*, 1349.
[16] M. Shahinpoor, K. J. Kim, M. Mojarrad, *Artificial Muscles: Applications Of Advanced Polymeric Nano-Composites*, Taylor and Francis-CRC, New York **2007**, ISBN 11-5848-8713-3.
[17] Foroughi, G. Spinks, *Nanoscale Adv.* **2019**, *1*, 4592.
[18] U. Kosidlo, M. Omastová, M. Micusík, G. Ćirić-Marjanović, H. Randriamahazaka, T. Wallmersperger, A. Aabloo, I. Kolaric, T. Bauernhansl, *Smart Mater. Struct.* **2013**, *22*, 104022.
[19] W. Wang, Y. Liu, J. Leng, *Coord. Chem. Rev.* **2016**, *38*, 320.
[20] B. Lester, T. Baxevanis, Y. Chemisky, D. Lagoudas, *Acta Mech.* **2015**, *226*, 3907.
[21] A. Miriyev, K. Stack, H. Lipson, *Nat. Commun.* **2017**, *8*, 596.
[22] L. Chang, D. Wang, A. Jiang, Y. Hu, *ChemPlusChem* **2022**, *87*, 202100437.
[23] C. S. Haines, N. Li, G. M. Spinks, A. E. Aliev, J. Di, R. H. Baughman, *Proc. Natl. Acad. Sci.* **2016**, *113*, 11709.
[24] P. Martins, D. M. Correia, V. Correia, S. Lanceros-Mendez, *Phys. Chem. Chem. Phys.* **2020**, *22*, 15163.
[25] S. M. Mirvakili, I. W. Hunter, *Adv. Mater.*,**2018**, *30*, 1704407.
[26] K. Asaka, H. Okuzaki, *Soft Actuators*, Springer, Berlin **2014**.
[27] F. Carpi, R. Kornbluh, P. Sommer-Larsen, G. Alici, *Bioinspiration Biomimetics* **2011**, *6*, 045006.

[28] K. J. Kim, S. Tadokoro, *Electroactive Polymers for Robotic Applications*, Springer, Berlin **2007**.
[29] L. Ionov, *Langmuir* **2015**, *31*, 5015.
[30] T. Mirfakhrai, J. D. W. Madden, R. H. Baughman, *Mater. Today* **2007**, *10*, 30.
[31] J. D. Madden, N. Vandesteeg, P. A. Anquetil, P. G. Madden, A. Takshi, R. Z. Pytel, S. R. Lafontaine, P. A. Wieringa, I. W. Hunter, *IEEE J. Oceanic Eng.* **2004**, *29*, 706.
[32] C. Majidi, *Adv. Mater. Technol.* **2019**, *4*, 1800477.
[33] Y. Tian, Y. Tao, H. Tian, Y. Yang, T.-L. Ren, *Soft Rob.* **2021**, *8*, 241.
[34] Y. Cao, J. Dong, *Soft Matter* **2021**, *17*, 2577.
[35] H. Shepherd, I. Gural'skiy, C. Quintero, S. Tricard, L. Salmon, G. Molnar, A. Bousseksou, *Nat. Commun.* **2013**, *4*, 2607.
[36] D. Manrique-Juarez, S. Rat, L. Salmon, G. Molnar, C. M. Quintero, L. Nicu, H. J. Shepherd, A. Bousseksou, *Coord. Chem. Rev.* **2016**, *308*, 395.
[37] P. Guionneau, *Dalton Trans.* **2014**, *43*, 382.
[38] M. Grzywa, R. Röß-Ohlenroth, C. Muschielok, H. Oberhofer, A. Błachowski, J. Żukrowski, D. Vieweg, H.-A. Krug von Nidda, D. Volkmer, *Inorg. Chem.* **2020**, *59*, 10501.
[39] *Spin Crossover in Transition Metal Compounds I-III* (Ed.: P. Gütlich, H. A. Goodwin), Springer, Berlin, Heidelberg **2004**.
[40] *Spin-Crossover Materials: Properties and Applications* (Ed.: M. A. Halcrow), John Wiley & Sons Ltd, Oxford, UK **2013**.
[41] *Spin Crossover Phenomenon* (Ed.: A. Bousseksou, C. R. Chimie), Vol. *21*, Académie des Sciences, Paris **2018**, pp. 1055–1300.
[42] A. Enriquez-Cabrera, A. Rapakousiou, M. Piedrahita Bello, G. Molnár, L. Salmon, A. Bousseksou, *Coord. Chem. Rev.* **2020**, *419*, 213396.
[43] J. E. Angulo-Cervera, M. Piedrahita-Bello, B. Martin, S. E. Alavi, W. Nicolazzi, L. Salmon, G. Molnar, A. Bousseksou, *Mater. Adv.* **2022**, *3*, 5131.
[44] A. Guralskiy, C. M. Quintero, J. Sa´nchez Costa, P. Demont, G. Molnar, L. Salmon, H. J. Shepherd, A. Bousseksou, *J. Mater. Chem. C* **2014**, *2*, 2949.
[45] M. D. Manrique-Juarez, F. Mathieu, A. Laborde, S. Rat, V. Shalabaeva, P. Demont, O. Thomas, L. Salmon, T. Leichle, L. Nicu, G. Molnár, A. Bousseksou, *Adv. Funct. Mater.* **2018**, *28*, 1801970.
[46] M. Piedrahita-Bello, J. E. Angulo-Cervera, A. Enriquez-Cabrera, G. Molnar, B. Tondu, L. Salmon, A. Bousseksou, *Mater. Horiz.* **2021**, *8*, 3055.
[47] M. Piedrahita-Bello, Y. Zan, A. Enriquez-Cabrera, G. Molnar, B. Tondu, L. Salmon, A. Bousseksou, *Chem. Phys. Lett.* **2022**, *793*, 139438.
[48] M. Piedrahita-Bello, J. E. Angulo-Cervera, R. Courson, G. Molnar, L. Malaquin, C. Thibault, B. Tondu, L. Salmon, A. Bousseksou, *J. Mater. Chem. C* **2020**, *8*, 6001.
[49] B. Tondu, M. Piedrahita-Bello, L. Salmon, G. Molnár, A. Bousseksou, *Sens. Actuators A* **2022**, *335*, 113359.
[50] H. Dong, J. Sun, X. Liu, X. Jiang, S. Lu, *ACS Appl. Mater. Interfaces* **2022**, *14*, 15504.
[51] Y. He, J. Guo, X. Yang, B. Guo, H. Shen, *RSC Adv.* **2021**, *11*, 37744.
[52] X. Ji, F. Gao, Z. Geng, D. Li, *Polym. Test.* **2021**, *97*, 107135.
[53] V. Y. Sirenko, O. I. Kucheriv, A. Rotaru, I. O. Fritsky, I. Gural'skiy, *Eur. J. Inorg. Chem.* **2020**, *2020*, 4523.
[54] A. Frick, A. Rochman, *Polym. Test.* **2004**, *23*, 413.
[55] G. Besendorfer, A. Roosen, *J. Am. Ceram. Soc.* **2008**, *91*, 2514.
[56] H. Watanabe, T. Kimura, T. Yamaguchi, *J. Am. Ceram. Soc.* **1989**, *12*, 289.
[57] M. Raj, S. M. Dunn, W. R. Cannon, *J. Comput. Assisted Microsc.* **1998**, *10*, 33.
[58] S. Timoshenko, *J. Opt. Soc. Am.* **1925**, *11*, 233.
[59] S. E. Alavi, B. Martin, Y. Zan, X. Yang, M. Piedrahita Bello, W. Nicolazzi, L. Salmon, G. Molnár, A. Bousseksou, Dynamical Mechanical Analysis and Micromechanics Simulations of Spin-Crossover@Polymer Particulate Composites: Towards Soft Actuator Devices **2023**, unpublished.
[60] R. Saeed, *Lyapunov Stability Theory with Some Applications*, Lap Lambert Academic Publishing, Chisinau, Moldova **2017**.
[61] M. Grzywa, A. O'Dwyer, *Handbook Of PI and PID Controller Tuning Rules*, 3rd ed., Imperial College Press, London, UK **2009**.
[62] L. G. Lavrenova, O. G. Shakirova, V. N. Ikorskii, V. A. Varnek, L. A. Sheludyakova, S. V. Larionov, *Russ. J. Coord. Chem.* **2003**, *29*, 22.